ARTICLE

Correlating Surface Structures and Electrochemical Activity Using Shape-Controlled Single-Pt Nanoparticles

Ke Huang, Kihyun Shin, Graeme Henkelman,* and Richard M. Crooks*

Read Online

ACCESS | Metrics & More | Article Recommendations | SI Supporting Information

ABSTRACT: We report a method for synthesizing and studying shape-controlled, single Pt nanoparticles (NPs) supported on carbon nanoelectrodes. The key advance is that the synthetic method makes it possible to produce single, electrochemically active NPs with a vast range of crystal structures and sizes. Equally important, the NPs can be fully characterized, and, therefore, the electrochemical properties of the NPs can be directly correlated to the size and structure of a single shape. This makes it possible to directly correlate experimental results to first-principles theory. Because just one well-characterized NP is analyzed at a time, the difficulty of applying a theoretical analysis to an ensemble of NPs having different sizes and structures is avoided. In this article, we report on two specific Pt NP shapes having sizes on the order of 200 nm: concave hexoctahedral (HOH) and concave trapezohedral (TPH). The former has {15 6 1} facets and the latter {10 1 1} facets. The electrochemical properties of these single NPs for the formic acid oxidation (FAO) reaction are compared to those of a single, spherical polycrystalline Pt NP of the same size. Finally, density functional theory, performed prior to the electrochemical studies, were used to interpret the experimental results of the FAO experiments.

KEYWORDS: single nanoparticle, carbon nanoelectrode, formic acid electrooxidation, density-functional theory, structure−function relation
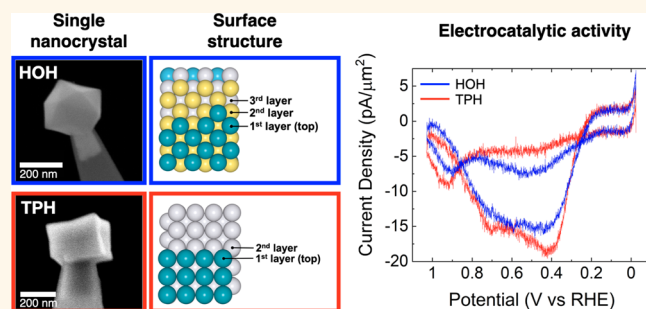
Here, we show that single Pt nanoparticles (NPs) having concave hexoctahedral (HOH), concave trapezohedral (TPH), and spherical shapes can be directly electrodeposited onto carbon nanoelectrodes (CNEs) by applying appropriate square-wave potential (SWP) programs. More importantly, these individual Pt NPs can be characterized by both electron microscopy and electrochemical methods to reveal their surface structures and electrocatalytic properties.

There are two specific aspects of this work that are significant. First, the electrosynthetic approach provides reproducible control over the size and structure of single Pt NPs. Second, because we have developed microscopic characterization methods for analyzing the NPs, it is possible to correlate their structure to their electrocatalytic properties. In a general sense, the most important aspect of our findings is that they provide a robust methodology for understanding electrocatalytic processes at NPs without the complexity of having to consider a distribution of heterogeneous materials. In other words, unambiguous correlations between the structures

and electrocatalytic properties of NPs can be made using the approach described here.

Not all surface structures on an electrocatalyst are equally active.[1−9] In fact, sometimes a slight change in structure can result in a drastic difference in the activity and selectivity of a catalyst for a specific reaction.[10] In contrast to bulk materials, however, where single-crystal electrodes with well-defined surface structures are available,[1,2,11−14] ensembles of catalytic NPs are always, at least to some extent, polydisperse.[7,8,15−17] That is, although there have been several improvements in NP synthetic methods that have served to narrow the degree of heterogeneity of NP ensembles, they are not perfect.[18−22] For understanding the fundamentals of catalytic reactions, this

17926

https://doi.org/10.1021/acsnano.1c06281
ACS Nano 2021, 15, 17926−17937
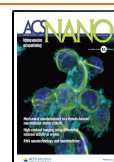
means that usually only an average structure can be correlated to an average function; the atomic-level details are, to some extent, subjugated by the heterogeneity of the ensemble. Indeed, a small subpopulation of NP structures can sometimes dominate catalytic activity.[23,24] To avoid the intrinsic heterogeneity discussed above, and hence to better understand the relationship between surface structure and catalytic activity for NPs, it is reasonable to explore the viability of studying reactions at individual, well-defined NPs. Here, we focus specifically on electrocatalysis at single NPs.

Several different approaches have been used to study the electrocatalytic properties of individual NPs. For example, the Bard group introduced the idea of single NP amplification, which makes it possible to measure the current produced at a single NP colliding the surface of a microelectrode.[25,26] The Zhang and Mirkin groups reported separately on electrochemical measurements of single Au NPs immobilized on the surfaces of nanoelectrodes.[27,28] The Unwin group, and subsequently others, used scanning electrochemical cell microscopy to map the electrochemical activities of individual NPs immobilized on different supporting electrode surfaces.[24,29,30] The Tao group[31] and the Chen group[32] used different spectroscopic methods to not only measure the catalytic activity of individual NPs, but also to obtain information about the size and/or location of the active sites on those NPs.

The aforementioned accomplishments have provided a first step toward the design of effective systems for making single-entity measurements and understanding the electrocatalytic properties of individual NPs. However, these studies also reveal two significant shortcomings. First, they usually require the use of surface ligands for shaping, stabilizing, and/or immobilizing NPs on electrode surfaces. These ligands can have complex effects on the electrocatalytic behavior of NPs, which are difficult to take into account when interpreting the results of experiments.[28,33,34] Second, it has proven to be difficult to obtain structural information about individual NPs after they are immobilized on an electrode. In fact, in most cases, there is no structural information at all. This makes it impossible to correlate structure and function using current methods for studying the electrocatalytic properties of individual NPs.

Our group previously showed that single, stabilizer-free Pt NPs having controlled sizes and shapes can be electro-deposited onto CNE surfaces using specific SWP programs.[35] This approach is a hybrid of a CNE fabrication method developed by Takahashi et al.[36] and later by Actis et al.[37] and the shape-controlled ensemble electrodeposition method introduced by Sun and co-workers.[19] In a preliminary report, we demonstrated that our electrodeposition approach resulted in individual, concave HOH Pt NPs having sizes ranging from 400 nm to 1000 nm. Importantly, the relative standard deviation for the size of these NPs was only 6%. We also showed that environmental scanning electron microscopy (ESEM), transmission electron microscopy (TEM), selected-area electron diffraction (SAED), and cyclic voltammetry (CV) can be used to characterize the surface structures and surface areas of individual NPs.

In the present article, we demonstrate that a judicious choice of electrodeposition conditions can lead to different Pt NP shapes and sizes as small as ~150 nm. Next, we show that the structures of these individual NPs can be characterized using ESEM, TEM, SAED, and a technique called coherent nanoarea

electron diffraction (NED). NED is a surface structure characterization method that was pioneered by the Petrov group[38] and the Zuo group.[39] It provides a means for determining the identity of specific surface facets on a NP without the need for manually mapping surface atoms from high-resolution TEM images. Finally, we demonstrate that the electrocatalytic properties of each shape and surface structure can be compared by studying the current responses during the electrochemical formic acid oxidation (FAO) reaction in both experiments and theory. This reaction and the hydrogen adsorption/desorption reaction used for surface area estimation are known to be highly structure sensitive on Pt.[13,15,40−44]

RESULTS AND DISCUSSION

Features of CNEs. Using the fabrication approach described in the Methods section, we obtained nanoelectrodes having tip openings of <80 nm (see Figure S1 in the Supporting Information (SI)). Interestingly, the carbon surface of these nanoelectrodes is not flush with the opening of the pipet, but rather it is usually recessed by ~300−500 nm.[45,46] The origin of this recession is uncertain, but it is a reproducible consequence of our fabrication method. In terms of the single Pt NP electrodeposition approach, a recessed carbon electrode surface means that electrodeposited Pt must fill the space above the carbon surface within the pipet before it can form a symmetrically shaped NP. This two-stage electrodeposition process (filling of the pipet tip followed by formation of the NP) has simplified exerting control over the size of the NPs and also benefited the stabilization of NPs on nanoelectrodes. These two points will be discussed in more detail in the following sections.

Electrosynthesis of Shape-Controlled Single Pt NPs. The micrographs in Figure 1 show typical images for three different shapes (HOH-, TPH-, and spherical-shaped in Figures 1a, 1b, and 1c, respectively) of single Pt NPs that were electrodeposited onto separate CNEs using the conditions described in the Methods section. The identity of the three shapes was determined by examining ESEM images of each Pt NP from different directions. The results indicate the shapes are HOH, TPH, and spherical. As discussed later, the shape of the Pt NPs is reproducible.

As alluded to earlier, there are two distinct stages of electrodeposition for the single Pt NPs. During the initial stage of electrodeposition, Pt fills the recessed space above the surface of the CNE (Figure 2a), and during the second stage the shaped Pt NP forms atop the Pt previously filled in the recessed region (Figure 2b). For all HOH and TPH NPs, both stages were performed using different and tightly controlled SWP programs. However, a simple CV scan was used in the second electrodeposition stage to prepare spherical NPs (as those shown in Figure 1c).[47] Because the electrodeposition methods are different for the polyhedral and spherical NPs in the second stage, it was necessary to develop a method for determining when to end the initial stage. We found that the best way to do this was to monitor the current, as a function of time, and stop the electrodeposition at a particular, easily determined point (Figure S2 in the SI).

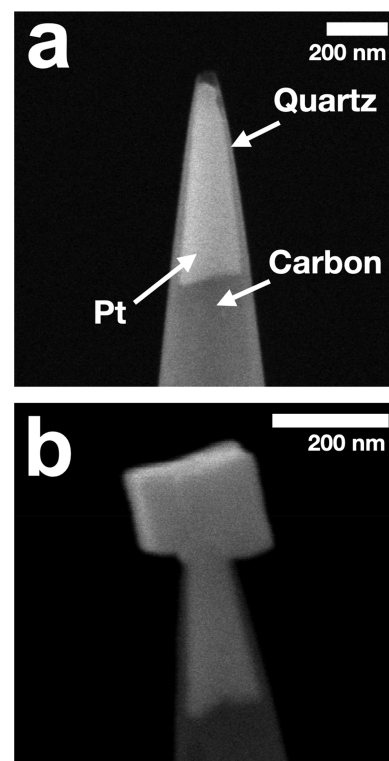For the HOH and TPH shapes shown in Figures 1a and 1b, respectively, electrodeposition was halted when predetermined cathodic and anodic current increases were achieved during the second (NP forming) electrodeposition stage. This makes it possible to control the NP size. On the basis of five independently prepared Pt NPs prepared using five independ-
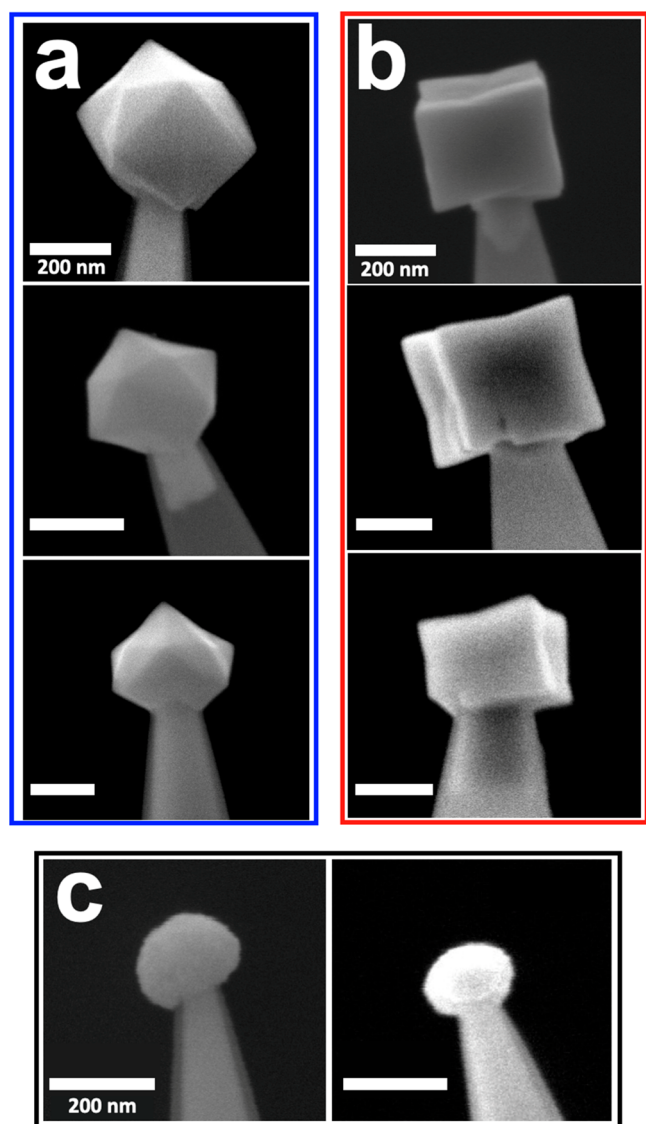
Figure 1. Replicates of the three shapes of single Pt NPs obtained using the shape-controlled electrodeposition method described in the Methods section: (a) HOH-shaped, (b) TPH-shaped, and (c) spherical-shape NPs.

Figure 2. SEM images of a CNE (a) after the initial stage of Pt electrodeposition in which only the recessed portion of the CNE has been filled and (b) after the second stage of Pt electrodeposition in which a Pt NP (TPH, in this case) forms atop the electrode.

ently fabricated electrodes, when the net increase in the cathodic current was controlled to be 0.27 nA, the size distributions of the NPs were 157 ± 4 nm (RSD = 3%) for the HOH shape and 176 ± 11 nm (RSD = 6%) for the TPH shape.

The spherically shaped Pt NPs, shown in Figure 1c, were obtained by scanning the electrode potential between 0.40 V and 1.20 V at 0.40 V/s during the second growth stage. The resulting current was monitored at the lowest potential (0.40 V), and the electrodeposition was halted when a current of 0.037 nA was achieved at this potential. The size distribution of the spherical Pt NPs was 171 ± 16 nm (RSD = 9%). Additional images of independently prepared Pt NPs, having each of the three shapes exemplified by those shown in Figure 1, are provided in Figure S3 in the SI. As would be expected for any electrodeposition process, the net increase in the cathodic current during electrodeposition is directly proportional to the size of the NP. To achieve well-resolved electrochemical measurements and microscopic images, we have used slightly

larger NPs for the remainder of this study: average sizes of 200 nm for HOH NPs and 230 nm for TPH NPs. The net current increase to obtain these sizes is ~0.4 nA. Finally, we note that the smallest size of single NPs that can be obtained using the electrodeposition approach described here is determined by the size of the CNE. Currently, we have not been able to electrodeposit NPs smaller than 100 nm reproducibly on the ~80 nm CNEs that we present herein.

Before addressing the analyses of single Pt NPs, we wish to briefly discuss a general aspect of the shape-controlled electrodeposition process. As suggested by the 0.04 V difference in lower limit potentials used for the fabrication of two of the shapes, the previously described SWP electrodeposition approach is extremely sensitive to potential limits. For example, a change as small as 0.02 V in either the upper or lower potential limit can alter the resulting NP geometry (see Figure S4 in the SI). Although such sensitivity could be beneficial for the purpose of achieving a wide variety of shapes, special care is required to ensure the fidelity of the reference potential to obtain reproducible results.

TEM and NED Analyses of Single Pt NPs. Correct correlation of electrochemical activities to the structures shown in Figure 1 requires structural characterization data of individual NPs. TEM is one of the most practical methods for resolving the structure of NPs,[48−50] but it has been found to be challenging to obtain high-resolution images of single NPs resting on the tip of nanoelectrodes.[27,28] This difficulty may be attributed to the fact that, in these earlier examples, the single NPs were much smaller than the size of the supporting electrodes. In our case, however, the Pt NPs are larger than the supporting CNEs, so the problem is, to some extent, simplified.

We have previously shown that both bright-field and high-resolution TEM are possible when imaging single Pt NPs having a critical dimension of ~500 nm.[35] This is also true for the ~200 nm NPs reported here; however, for these smaller NPs, the imaging success rate is lower. As discussed next, we think this is mostly due to surface charging effects that are attributable to the TEM beam.

Figure 3 is the TEM image of a HOH Pt NP confined to the tip of a CNE. The procedure for preparing these electrode/NP
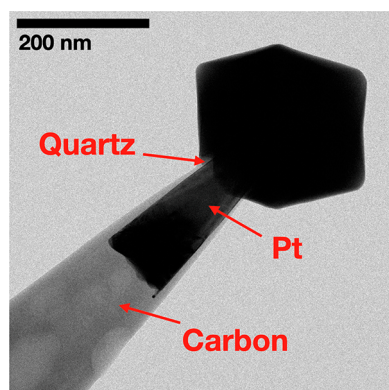

Figure 3. Bright-field TEM image of a HOH Pt NP. The image clearly shows the relationship between the NP, Pt within the recessed region of the CNE, the carbon base of the electrode, and the quartz sheath.

samples for TEM analysis is straightforward but exacting; a detailed procedure is provided in Figure S5 in the SI. One unfortunate aspect of the mounting method is that the distal Pt NP is not in electrical contact with the TEM grid to which it is attached, nor is it in contact with the TEM holder. Under these circumstances, charging of the NP by the electron beam is hard to avoid. Besides specimen drift caused by the charging, we have noticed that the single NPs occasionally change shape or fly off the tip of the electrode under the beam at 200 kV. We have also noticed that when the depth of Pt within the recessed region of the CNE is >250 nm, the attached Pt NP is more stable under the TEM beam. Nevertheless, drift is still difficult to avoid. These problems have limited our high-resolution transmission electron microscopy (HRTEM) imaging success rate, so we have employed NP surface characterization methods that require only bright-field and diffraction imaging, specifically, projection angle analysis[7,49,51] and NED,[38,39,52,53] as our primary surface characterization methods.

Projection angle analysis relies on measurement of projection angles for a specific shape of NP from a predetermined imaging direction. These experimentally determined values are then compared to those predicted by theory for different {hkl} combinations. Equations for calculating theoretical projection angles for both the HOH and TPH shapes are provided in Table S1 in the SI.

Figure 4a presents the projection angle results for a typical TPH NP on the [100] zone axis. The measured projection angles obtained using two independently prepared Pt NPs were 78.7 ± 0.4° and 168.6 ± 1.9°, which match well with those predicted for {10 1 1} facets. A geometric model of the TPH shape oriented on the [100] zone axis and the corresponding projection angles on the model are shown on the right side of the figure. A simulated model for this facet is shown in Figure 4b. HRTEM images of the TPH NP,
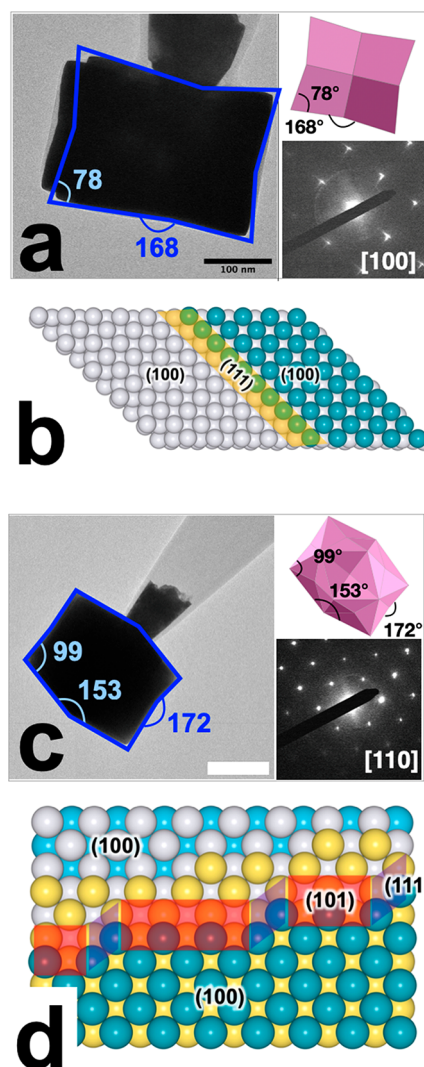
Figure 4. Projection angle analysis for (a, b) TPH and (c, d) HOH NPs after electrochemical cleaning. Bright-field TEM images, corresponding shape model, and SAED pattern recorded from the [100] direction for the TPH shape (panel (a)), and the [110] direction for the HOH shape (panel (c)). Panels (b) and (d) are simulated atomic models for {10 1 1} and {15 6 1} surface facets, respectively.

discussed later, were also analyzed, and further validate this surface facet assignment.

An analysis similar to that shown in Figure 4a was performed for the HOH NPs on the [110] zone axis (Figure 4c). A geometric model of the HOH shape and the corresponding projection angles are shown on the right. The average values for the angles obtained using four independently prepared Pt NPs were 152.7° ± 1.0°, 100.2° ± 1.0°, and 171.2° ± 1.7°, which are in close agreement with those predicted for {15 6 1} facets. As a result, we conclude that the HOH NPs are bound by {15 6 1} surface facets, which are represented in Figure 4d.

To better understand the HOH NPs, NED analysis was performed on the [110] zone axis, and the result is presented in Figure S6 in the SI. Figure S6a in the SI is the NED pattern over the entire area shown in Figure S6b in the SI. A magnified view of the secondary diffraction pattern and the direction of each streak in that pattern obtained at the ($\bar{2}$20) diffraction spot is shown in Figure S6c in the SI. Although the NED

technique can be powerful for characterizing the surface structure of a NP having a complex shape, it can only correctly describe the surface facet when that surface is perfectly parallel to the beam. In the case of the HOH shape, none of the NP surfaces can be parallel to the beam on any of the three low-index imaging axes ([100], [110], or [111]), which makes it difficult to use NED to reveal the exact surface atomic arrangement. However, the long and sharp streaks in the secondary pattern (Figure S6c) indicate that the HOH NP likely has a dominant surface facet containing small numbers of defects.[39] The dominant facet, as determined by the angle measurements using both TEM projections and NED patterns, is {15 6 1}.

Figure 5a shows a TPH NP imaged on the [110] zone axis, as confirmed by the diffraction pattern in Figure 5b. Although
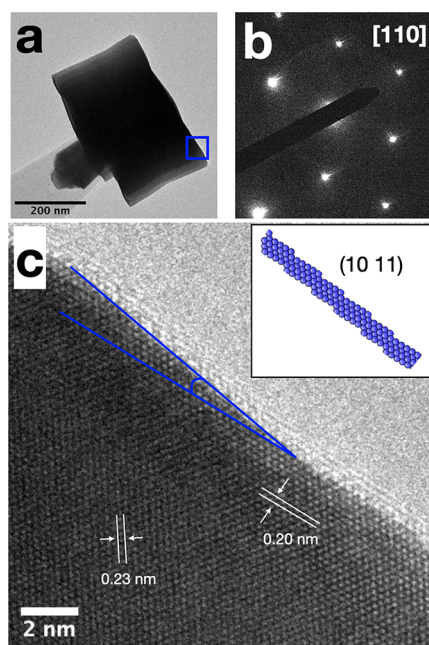

Figure 5. (a) TEM image of an electrochemically cleaned TPH-shaped Pt NP. (b) Diffraction pattern for the particle in panel (a) confirming that it was imaged along the [110] zone axis and is a single-crystal NP. (c) An HRTEM image of the region in panel (a) defined by a blue box. The measured lattice spacings reflecting the [110] imaging direction. The angle measured between the (100) plane and the surface (as illustrated by the blue lines) is 7.9°, which matches well with that measured on {10 1 1} surface. Inset shows the {10 1 1} surface viewed from the [110] direction and rotated to match the lattice direction in the HRTEM image.

the resolution of the HRTEM image (as shown in Figure 5c) is not ideal for atomic mapping, we were able to resolve the {10 1 1} surface faceting by measuring the angle between the (100) lattice plane and the surface, which is 7.9°. Therefore, we conclude that {10 1 1} is the surface facet present on the TPH Pt NPs.

Analysis of Single Pt NPs by H Adsorption/Desorption. H adsorption/desorption cyclic voltammograms (henceforth, H CVs) may be used to provide information about the surface features and surface areas of single Pt NPs.[47,54] The main purpose of this part of the study is to determine the surface areas of the single NPs, but we also show that the surface faceting is in general qualitative agreement with the foregoing microscopy analysis.

As discussed in the Methods section, all NPs were cleaned in a 0.50 M H_2SO_4 solution by scanning the electrode potential between −0.03 V and 1.20 V at 1.00 V/s before electrochemical measurements and microscopic imaging. We used H_2SO_4 as the electrolyte for this analysis, rather than $HClO_4$, which is also in common use for this purpose, because it led to better-defined H adsorption/desorption peaks.[18] This cleaning process was stopped when the voltammetric response from a NP remained unchanged for at least three cycles. Subsequently, two consecutive H CVs were recorded between −0.03 V and 1.20 V, using a scan rate of 0.40 V/s. The active surface area of each NP was then calculated by integrating the charge under the H adsorption peaks between −0.01 V and 0.40 V, and then converting this charge to surface area, assuming a charge density of 230 $\mu C/cm^2$. The latter value has been used by other groups for analyzing the surface areas of shape-controlled Pt NPs.[54,55]

Figure 6 shows surface area-normalized, background-subtracted, and smoothed voltammetric responses obtained
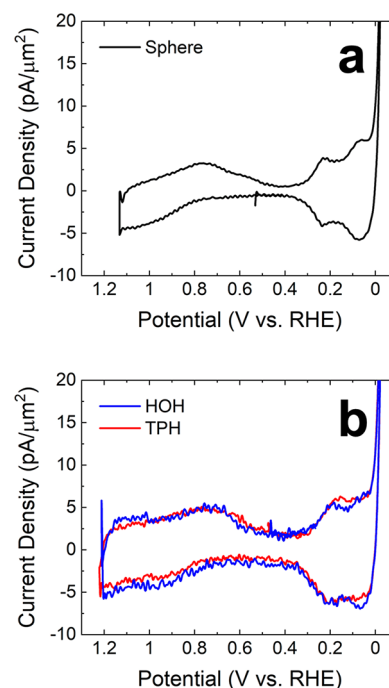
Figure 6. (a) An H CV for spherical single Pt NP. (b) H CVs for TPH and HOH single Pt NPs. The CVs were obtained in 0.5 M H_2SO_4. The scan rate was 0.40 V/s, and the data were smoothed using the (a) 45-point and (b) 25-point FFT filters in OriginLab. The unsmoothed data are provided in Figures S7b and S7c in the SI.

using spherical (Figure 6a, black), TPH (Figure 6b, red), and HOH (Figure 6b, blue) Pt NPs during the second cycle of the H CVs. A representative example of the raw data from which these CVs were extracted, including a background CV used for subtraction, is provided in Figure S7a in the SI. The unsmoothed data from which the CVs in Figure 6 originated are provided in Figures S7b and S7c in the SI. For spherical and HOH NPs, two pairs of peaks are clearly visible in the H region between −0.01 V and 0.40 V. The peak separation for the TPH NPs is not as clear, which is likely a consequence of the peaks being closer to each other for the TPH NPs.

The pairs of peaks at ∼0.20 V and ∼0.07 V should correspond to H adsorption/desorption on the (100) and (110) facets, respectively.[55,56] The height of the peak near 0.20 V is higher for both the HOH and TPH NPs than for the spherical NPs. This trend is consistent with previous reports for H adsorption on ensembles of Pt NPs having similar well-defined surface structures[55,57] and on macroscopic Pt surfaces having similar high-index facets.[13] This indicates that the HOH and TPH NPs discussed here also have high-index facets (as confirmed by the electron microscopy discussed earlier).

Electrocatalytic Activity of Single Pt NPs: Experimental Considerations. One of our reasons for developing a well-defined, single-NP system is to devise models for better understanding the structure−function relationship of NP catalysts. Accordingly, we sought to examine the electrocatalytic responses of the three NP shapes for electrochemical formic acid oxidation (FAO) reaction. Even though these electrocatalytic results are discussed at this point, the measurements were actually performed prior to structural analysis (because the CNEs must be broken for TEM analysis). We chose the FAO because it is known to be sensitive to the surface structure of Pt NPs.[15,40,51,58−60] CVs for the single NPs were obtained using a solution containing 0.50 M HCOOH and 0.10 M HClO$_4$, and by cycling the potential between 0 and 1.02 V at a scan rate of 0.10 V/s.[41,61,62] We analyzed some electrodes before the FAO and some after, and there were no observable differences in the surface structure. We conclude that FAO cycling scans do not result in scrambling of the Pt surfaces.

A dual-path reaction mechanism is usually assumed for the FAO on Pt: a direct pathway through active intermediates and an indirect pathway through surface-adsorbed CO.[41,63,64] To illustrate this mechanism, Figure 7a shows a typical cyclic voltammogram for FAO on a polycrystalline Pt ultramicroelectrode (UME). The scan starts at 0 V and continues in the direction indicated by the arrow. At 0 V, the Pt surface is partially poisoned by a CO adlayer (CO*) resulting from decomposition of formic acid at low potential. As the scan continues in the positive direction, the fraction of the Pt surface not poisoned by CO* starts to electrocatalyze the oxidation of formic acid to CO$_2$, which leads to a current peak (Peak 1) at ∼0.56 V. At potentials more positive than 0.73 V, CO* is oxidized, which unblocks those previously poisoned Pt sites and makes them available for further FAO electrocatalysis (Peak 2).[15]

As the potential becomes even more positive, surface Pt atoms start to oxidize and, hence, lose their ability to catalyze the FAO. This leads to the current decrease above ∼0.86 V. It has previously been shown that higher reversal potentials lead to more surface recovery from CO poisoning due to CO* oxidation and, hence, higher current responses for the FAO upon scan reversal.[54] Considering that higher potentials may also lead to disruption of the original surface structure, however, we chose to stop the positive-going scan at 1.02 V, which is the same reversal potential used to obtain the H CVs.[65]

Upon scan reversal, the catalytic Pt surface reactivates due to reduction of surface oxides. This leads to a broad maximum in the current arising from direct FAO at ∼0.55 V (Peak 3). At potentials more negative than this value, CO* again deposits onto the Pt surface, so the direct FAO reaction begins to shut down, and the current decreases. As a result, current responses obtained in the negative-going scan reflect the intrinsic activity
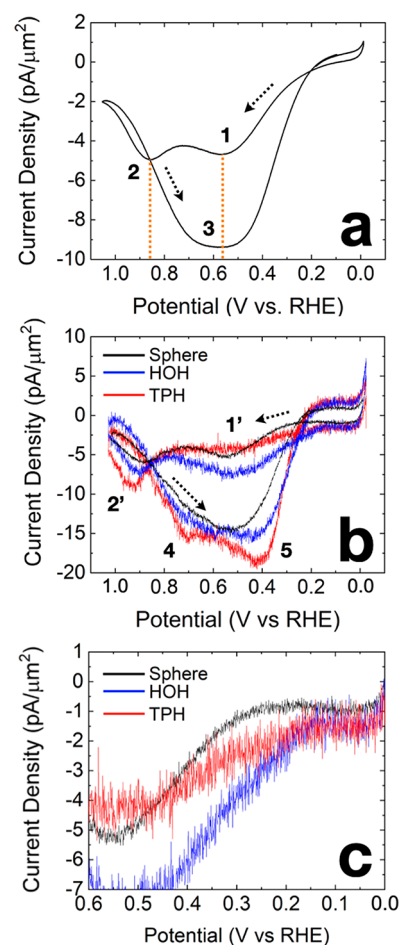
Figure 7. (a) CVs for the FAO obtained using a 12.5 µm Pt UME. (b) CVs for the FAO on spherical, HOH, and TPH single Pt NPs. (c) Expanded view of the onset potential region for the three shapes. All FAO CVs were obtained in a solution containing 0.50 M HCOOH and 0.10 M HClO$_4$. Scan rates were 0.02 V/s in panel (a) and 0.10 V/s in panel (b). Arrows indicate the scan directions.

of the Pt surface through the direct pathway(s) only. Accordingly, the ratio between the current densities at Peaks 1 and 3 reflect the degree of CO poisoning on specific Pt surfaces.[15,55] Note that all of the features and peak positions shown in Figure 7a are in agreement with those previously reported for FAO on polycrystalline bead Pt electrodes in HClO$_4$ solutions.[40]

Figure 7b shows a comparison of representative CV scans for the FAO reaction performed on the three different-shaped single Pt NPs. Measurements for each shape were repeated three times using independently prepared single Pt NPs. Cyclic voltammograms obtained using the replicate HOH and TPH-shaped electrodes are consistent with those in Figure 7b and are provided in Figure S8 in the SI.

All of the cyclic voltammograms for the single Pt NPs exhibit the general features expected for the FAO on Pt, but there are also some important differences. In the case of the spherical, polycrystalline Pt NP (black), the voltammetric profile is very similar to that of the polycrystalline Pt UME (Figure 7a), but with a slightly greater degree of CO poisoning.

In the cases of the HOH (blue data in Figure 7) and TPH (red data in Figure 7) NPs, however, the voltammetric profiles are more complex. Specifically, on the reverse scan, a clear peak at 0.42 V (Peak 5) and a shoulder at 0.70 V (Peak 4) are

observed for both polyhedral-shaped NPs (Figure 7b), with the peak definition being clearer for the TPH shape. The positions of Peaks 4 and 5 have been associated with the FAO proceeding on Pt(110) sites (or defect sites) and Pt(100) terrace sites, respectively.[54,65]

The difference in the positions of Peak 3 (for the spherical single Pt NP) and Peak 5 (for the polyhedral single Pt NPs) is 0.13 V. This shift indicates that the polyhedral NPs have significant amounts of Pt(100) surface terrace sites. This observation is in accord with the surface facet models shown in Figures 4b and 4d (which are discussed in further detail in Figures S9 and S10 in the SI), where both {15 6 1} (HOH NPs) and {10 1 1} (TPH NPs) surfaces have Pt(100) terrace stackings. Indeed, the only difference between the facets on the HOH and TPH Pt NPs is in the structure of the step sites. Steps on the {15 6 1} facet have an asymmetric zigzag pattern with alternating Pt(111) and Pt(101) arrangements. However, the steps on the {10 1 1} facet are composed solely of Pt(111) arrangements.

In terms of current densities for the FAO reaction, the HOH and TPH NPs reveal higher reaction activities, compared to spherical NPs, but the increase is relatively small (~6% for the HOH NPs and ~26% for the TPH NPs). However, all three shapes of single Pt NPs exhibit significantly higher current densities than that obtained from the Pt UME, with the increase ranging between ~53% to ~118%. Although the difference in the current densities obtained between shapes is small, the onset potential for the direct oxidation process improves with HOH and TPH NPs (Figure 7c). Here, we define the onset potential of oxidation as the potential at which 10% of the current density of Peak 1' is achieved.[66] With this definition, we find that the onset potential for oxidation to be 0.19, 0.20, and 0.29 V for the HOH, TPH, and spherical NPs, respectively. The ~0.10 V negative shift in the onset potentials for HOH and TPH NPs show that the high-index surfaces are more active for the FAO reaction at low potentials.

As discussed earlier, CO* can act as an inhibitor or intermediate for the FAO reaction on Pt surfaces, depending on the applied potential. The degree of surface poisoning by CO* is usually assessed by comparing the highest current density achieved at ~0.55 V in the positive-going scan (i_{pos}) with that achieved at ~0.40 V (or 0.50 V for the spherical single Pt NPs) in the negative-going scan (i_{neg}). The smaller the ratio of i_{pos}/i_{neg}, the higher the degree of CO poisoning. Our results indicate that the TPH Pt NPs reproducibly exhibit more significant CO poisoning than the HOH shape. Specifically, $i_{pos}/i_{neg} = 0.33 \pm 0.05$ for HOH but only 0.18 ± 0.05 for the TPH shape. This indicates that the {10 1 1} surface is more subject to CO poisoning.

To confirm the foregoing conclusion, we mimicked CO poisoning during the FAO reaction by immersing the single NPs in a solution containing 0.50 M HCOOH and 0.10 M HClO$_4$ and then held their potential at 0.18 V for 40 s. Adsorbed CO* was then stripped by scanning the potential from 0.18 V to 1.02 V at 0.40 V/s in a 0.50 M H$_2$SO$_4$ solution. Figure S11 in the SI shows the outcome of this experiment for all three shapes of single Pt NPs. The results show that the TPH shape exhibits the highest degree of poisoning. Specifically, charge densities correspond to CO stripping are 0.46 pC/μm^2, 0.58 pC/μm^2, and 0.32 pC/μm^2 for spherical, TPH, and HOH NPs, respectively. Furthermore, the stripping potential for the TPH and HOH NPs are similar (both near 0.87 V), which is higher than that for the spherical NPs (0.74

V), suggesting (1) stronger CO* binding on the high-index surfaces and (2) similar CO* binding environments on the {15 6 1} and {10 1 1} surfaces. The latter point shows once more the similarity between the two high-index surfaces, in terms of their electrocatalytic properties for the FAO. As discussed next, such similarity is also predicted by density functional theory (DFT) calculations.

Electrocatalytic Activity of Single-Pt NPs: Theoretical Considerations. To further our understanding of the FAO reaction on the different-shaped single Pt NPs, we used DFT calculations to simulate FAO activities on the {15 6 1} and {10 1 1} surfaces. We wish to emphasize that these calculations were performed prior to the FAO experiments described in the previous section.

Figure 8 illustrates the four surfaces that we considered for simulations. The Pt(100) (Figure 8a) and Pt(111) (Figure 8b)
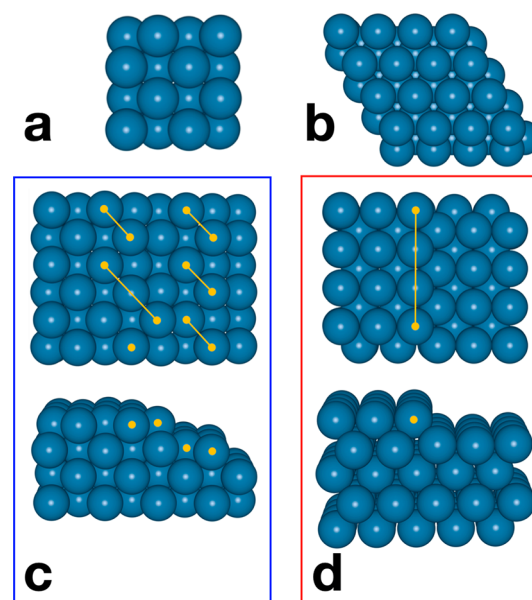
Figure 8. Illustrations of different surface slab models: (a) (100), (b) (111), (c) {15 6 1}, and (d) {10 1 1} surfaces. Upper figures in panels (c) and (d) are the top view, and the lower figures are the side view. Orange lines and dots represent step sites of the given surface.

surfaces are used as models for the polycrystalline Pt NP surface. Pt(111) was chosen because it is the most stable surface, in terms of surface energy, on Pt NPs. Pt(100) was chosen because it was found to be very active in catalyzing the FAO.[40,54,59] Figures 8c and 8d show the top (upper) and side views (lower) of {15 6 1} and {10 1 1} surfaces, respectively. In the simulation, three different FAO reaction mechanisms were considered: direct oxidation, through HCOO* or COOH* intermediates, and indirect oxidation, through surface poisoning by CO*.[41,67] Computational details and equations for each pathway are provided in the SI.

To start, we calculated the binding energies of the three intermediates (HCOO*, COOH*, and CO*) for the four surfaces shown in Figure 8. Comparing to the two low-index facets, the high-index, stepped surfaces ({15 6 1} and {10 1 1}) exhibit much stronger intermediate binding energies, as shown in Table 1. Using the calculated binding energies, reaction energy diagrams for each surface with each of the three reaction mechanisms were generated and are shown in Figures

Table 1. Binding Energies of the Three Intermediates Considered for the FAO Reaction on Different Surfaces

	Binding Energy			
	(100)	(111)	{15 6 1}	{10 1 1}
CO*	−1.204	−0.898	−1.339	−1.287
HCOO*	0.504	0.778	0.111	0.100
COOH*	0.324	0.409	0.022	−0.070

S12−S15 in the SI. The results from these calculations are presented next.

For the mechanism involving the HCOO* intermediate, the initial steps (formation of HCOO*) on every Pt surface are endothermic and HCOO* always adsorbed weakly to the surface; forming a relatively stable intermediate becomes the rate-determining step (RDS). Through this reaction mechanism, the results predicted lower overpotentials for the FAO for both {15 6 1} and {10 1 1} surfaces (0.41 and 0.40 V, respectively) than for the (100) and (111) surfaces (0.80 and 1.07 V, respectively). However, the difference between the two high-index surfaces is not significant. A similar result is predicted for the COOH*-intermediate formation mechanism: lower overpotentials are required for the high-index surfaces.

As shown by the very negative binding energies in Table 1, CO* binds strongly to all of the modeled surfaces. As a result, all surfaces should suffer from severe CO poisoning at low potentials, which agrees well with our experimental observations. With regard to the two high-index surfaces, our calculations suggest that the {15 6 1} surface should also provide a wider variety of possible surface sites to which FAO reaction intermediates can bind. In turn, a wider variation in possible binding sites should lead to a greater variation in binding energies, which could explain the more poorly defined peaks (at 0.42 and 0.70 V; see Figure 7b) in the reverse scan for the HOH NPs, compared to the TPH NPs.

Among the three different reaction mechanisms, the COOH* formation pathway is calculated to be the most favorable. Figure 9 summarizes the FAO reaction activities for the COOH* mechanism for all four surfaces. As indicated by the overpotentials (η), the (100) and (111) surfaces exhibit similar overpotentials, even though they have very different activities for the other direct pathway (through HCOO* formation). We believe this is because of the different bonding configurations of COOH* and HCOO* on these basal surfaces. HCOO* usually binds on the metal surface by making a bridge using its two O atoms,[68] so the surface intermetallic bond length is critical in the consideration of the binding energy of this intermediate.

However, COOH* usually uses its only C atom to bind on top of a metal atom (see Figures 9a and 9b), so the surface intermetallic bond length is not as important in this case. For the high-index surfaces, high surface energies at the step atoms allow both the carbon and oxygen in COOH* to be involved in the binding process. Although {15 6 1} and {10 1 1} exhibit similar binding energies, because of similar bonding configurations of the intermediate (Figures 9c and 9d), they have ∼0.30−0.48 V lower overpotential than the (100) and (111) surfaces. This overpotential difference is greater than the difference in the onset potential for oxidation observed experimentally (ca. 0.10 V). Considering that the calculations assume perfect surfaces in the absence of disorder or surface-adsorbed species, such as CO*, which are inevitable in experiments, the DFT results are in reasonable agreement with the experimental findings. Further analysis on the intrinsic activity of each surface structure for the FAO reaction, in the absence of CO poisoning, requires studies using techniques such as pulsed voltammetry. Such studies are beyond the scope of this report but should be readily achievable through the general methodology that we have presented here.

SUMMARY AND CONCLUSIONS

The key result in this article is that we have correlated a detailed structural analysis of a single Pt NP electrode to electrocatalytic results. This is significant because it makes direct correlation between experimental findings and theory possible.

Specifically, we have shown that shaped, single Pt NPs with diameters on the order of 200 nm can be electrodeposited
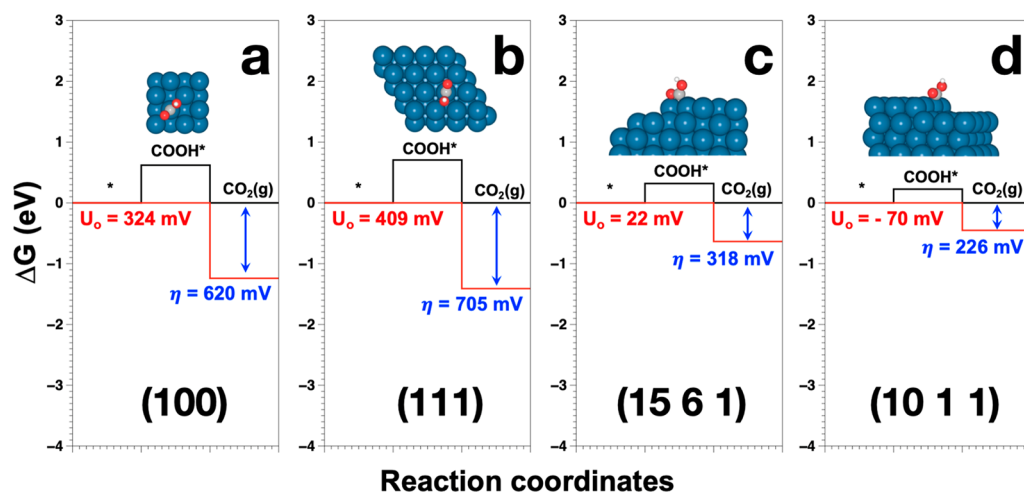
Figure 9. DFT calculated energy diagrams for the Pt(100), (111), (15 6 1), and (10 1 1) surfaces, assuming the reaction proceeds under the COOH* formation mechanism. Inset figures represent the bonding configuration of the COOH* intermediate on each surface. Here, the black lines represent the Gibbs free energies at equilibrium potential (U_{eq}), the red lines show results at the onset potential (U_o), where all of the reaction steps turn out to be exothermic, and we determined the catalytic activity of the FAO reaction by calculating the overpotential (η) with eq 8 listed in the SI.

onto CNEs with a high degree of control and reproducibility. An important result is that very small differences, just tens of millivolts, in the upper and lower square-wave potentials leads to very different single-NP structures. Accordingly, the basic methodology reported here should be broadly applicable to developing a better understanding of the structure−function relationship of NPs for electrocatalytic reactions.

Importantly, the DFT calculations, which were performed prior to the FAO experiments, demonstrate a good degree of correlation with the experimental observations. Specifically, we developed {15 6 1} and {10 1 1} slab models based on experimental structural analysis and compared their activities for the FAO reaction with Pt (100) and Pt (111) surfaces. The HCOO*, COOH*, and CO* formation pathways for the FAO reaction were then compared, and the COOH* formation mechanism was predicted to be the most favorable. High-index surfaces were calculated to have much lower overpotentials for FAO than the low-index surfaces, because step atoms in the high-index surfaces effectively stabilize the intermediates.

Moving forward, we plan to expand the scope of the findings reported here by examining both alternative shapes and other surface-sensitive reactions. We are also interested in the mechanism of NP growth, and, in particular, why such small changes in the potential program used for electrodeposition result in such different single-crystal shapes. The results of these studies will be reported in due course.

METHODS

Chemicals and Materials. K_2PtCl_4 (99.99% trace metal basis, Millipore Sigma), H_2SO_4 (OmniTrace, Ultra grade, Millipore Sigma), $HClO_4$ (70%, Fisher), and HCOOH (88%−90%, Millipore Sigma) were used as received. All solutions were prepared using deionized (DI) water (18.2 MΩ cm) from a Milli-Q system (Millipore Sigma).

Fabrication of CNEs. A quartz capillary (1.0 mm × 0.7 mm, Sutter Instruments) was pulled into two quartz nanopipettes, using a P-2000 laser puller (Sutter Instruments). Parameters for the laser puller were HEAT 720, FIL 3, VEL 25, DEL 135, PUL 150. The resulting quartz nanopipettes had tip lengths of ~6 mm. The larger end of each nanopipette was connected to an acetylene gas cylinder (dissolved in acetone, Praxair). The nanopipette was clamped horizontally and capped by a second quartz capillary (1.0 mm × 0.7 mm) connected to an argon cylinder (99.999%, Praxair). The flow rate of the argon was precisely controlled by a flowmeter (Dwyer), and a gentle argon flow of 60 sccm through the second capillary was used to prevent bending and cracking of the quartz nanopipette tip. The flame of a butane torch (Dremel) was configured so that the flame covered the tip of the nanopipette, resulting in pyrolysis of the flowing butane/propane mixed gas. The temperature of the flame was measured using a Type K thermocouple (Omega) and was adjusted to be ~1020 °C. A TEM image of a typical CNE is shown in Figure S1 in the SI.

Electrochemistry. All electrochemical reactions and measurements were performed in a two-electrode cell outfitted with a CNE working electrode and a leak-free Ag|AgCl (3.4 M KCl) miniature reference electrode (eDAQ). This reference electrode was calibrated against a Hg|Hg₂SO₄ (saturated K_2SO_4) reference electrode, and it was found to be −294 mV vs Hg|Hg₂SO₄ or 356 mV vs RHE at pH 0. Hereafter, all potentials are reported vs RHE.

Square-wave potentials were created using a function generator (BK Precision). For other electrochemical measurements, the necessary potential waveform was obtained using a universal programmer (EG&G, Model 175). All potentials and currents were processed through a Chem-Clamp (Dagan), and the results were recorded using a Labview program. The electrochemical current was unfiltered, and the gain was 1 mV/pA on the Chem-Clamp.

Shaped Single-Pt NP Electrodeposition. Electrodeposition was performed in solutions containing 2.0 mM K_2PtCl_4 and 0.10 M H_2SO_4. HOH and TPH Pt NPs were electrodeposited using a one-step SWP program with a frequency of 1.00 kHz but different potential limits. Specifically, HOH Pt NPs were electrodeposited using potentials that switched between 1.48 V and 0.19 V, while concave TPH Pt NPs were electrodeposited using 1.48 and 0.23 V. The accuracy of these potentials is crucial to the successful deposition of particular shapes.

Spherical Pt NPs were prepared as follows. Pt was electrodeposited using the same SWP treatment conditions used for HOH NPs, but only enough Pt was deposited to fill a recessed space in the nanopipette (see the SI for details). Next, additional Pt was electrodeposited by performing continuous CV scans that started at 0.55 V, went positive to 1.20 V, and then negative to 0.40 V at a scan rate of 0.40 V/s. This process resulted in single, spherical, polycrystalline Pt NPs.

Electron Microscopy. ESEM images of CNEs and Pt NPs were acquired using a FEI Quanta 650 microscope at either 10.0 kV or 15.0 kV with a spot size of 3.0. Each CNE having a single Pt NP on its tip was glued to a Cu slot grid (Ted Pella), using M-Bond 610 Curing Agent (Micro Measurements), so that the single-Pt NP was at the center of the hollow slot. The rest of the CNE was then cut so the sample could fit into a double-tilt TEM holder that allows both x- and y-directional tilting of ~15° (JEOL). A more-detailed TEM sample preparation procedure is provided in Figure S5 in the SI. TEM, SAED, and NED imaging of Pt NPs was then performed, using a JEOL Model 2010F microscope at 200 kV. It is important to mention that all single NPs undergo cleaning scans in 0.50 M H_2SO_4 solution between −0.03 V and 1.20 V at 1.00 V/s for 6−8 cycles before imaging.

ASSOCIATED CONTENT

ⓢ Supporting Information

The Supporting Information is available free of charge at https://pubs.acs.org/doi/10.1021/acsnano.1c06281.

TEM of CNE (Figure S1); current traces obtained during electrodeposition (Figure S2); ESEM images of HOH and TPH shapes of single Pt NPs (Figure S3); NP geometry change due to small potential change (Figure S4); TEM sample preparation (Figure S5); projection angle analysis equations (Table S1); NED results (Figure S6); raw and unsmoothed CVs for hydrogen adsorption/desorption (Figure S7); FAO CV replicates for different shapes of single Pt NPs (Figure S8); {15 6 1} facet and modeling (Figure S9); {10 1 1} facet and modeling (Figure S10); CO-stripping CVs for different shapes of single Pt NPs (Figure S11); computational details; energy diagrams for all considered surfaces through three different pathways (Figures S12−S15) (PDF)

AUTHOR INFORMATION

Corresponding Authors

Graeme Henkelman − *Department of Chemistry, Texas Materials Institute, and Oden Institute for Computational Engineering and Science, The University of Texas at Austin, Austin, Texas 78712-1224, United States;* ⓞ orcid.org/0000-0002-0336-7153; Email: henkelman@utexas.edu

Richard M. Crooks − *Department of Chemistry and Texas Materials Institute, The University of Texas at Austin, Austin, Texas 78712-1224, United States;* ⓞ orcid.org/0000-0001-5186-4878; Email: crooks@cm.utexas.edu

Authors

Ke Huang − *Department of Chemistry, The University of Texas at Austin, Austin, Texas 78712-1224, United States*

Kihyun Shin − *Department of Chemistry, The University of Texas at Austin, Austin, Texas 78712-1224, United States;* ⊙ orcid.org/0000-0002-1748-8773

REFERENCES

(1) Zambelli, T.; Wintterlin, J.; Trost, J.; Ertl, G. Identification of the "Active Sites" of a Surface-Catalyzed Reaction. *Science (Washington, DC, U. S.)* **1996**, *273*, 1688−1690.

(2) Pfisterer, J. H. K.; Liang, Y.; Schneider, O.; Bandarenka, A. S. Direct Instrumental Identification of Catalytically Active Surface Sites. *Nature* **2017**, *549*, 74−77.

(3) Ding, K.; Gulec, A.; Johnson, A. M.; Schweitzer, N. M.; Stucky, G. D.; Marks, L. D.; Stair, P. C. Identification of Active Sites in CO Oxidation and Water-Gas Shift over Supported Pt Catalysts. *Science (Washington, DC, U. S.)* **2015**, *350*, 189−192.

(4) Chang, L. Y.; Barnard, A. S.; Gontard, L. C.; Dunin-Borkowski, R. E. Resolving the Structure of Active Sites on Platinum Catalytic Nanoparticles. *Nano Lett.* **2010**, *10*, 3073−3076.

(5) Back, S.; Yeom, M. S.; Jung, Y. Active Sites of Au and Ag Nanoparticle Catalysts for CO₂ Electroreduction to CO. *ACS Catal.* **2015**, *5*, 5089−5096.

(6) Nørskov, J. K.; Bligaard, T.; Rossmeisl, J.; Christensen, C. H. Towards the Computational Design of Solid Catalysts. *Nat. Chem.* **2009**, *1*, 37−46.

(7) Yu, Y.; Zhang, Q.; Liu, B.; Lee, J. Y. Synthesis of Nanocrystals with Variable High-Index Pd Facets through the Controlled Heteroepitaxial Growth of Trisoctahedral Au Templates. *J. Am. Chem. Soc.* **2010**, *132*, 18258−18265.

(8) Lee, I.; Delbecq, F.; Morales, R.; Albiter, M. A.; Zaera, F. Tuning Selectivity in Catalysis by Controlling Particle Shape. *Nat. Mater.* **2009**, *8*, 132−138.

(9) Koper, M. T. M. Structure Sensitivity and Nanoscale Effects in Electrocatalysis. *Nanoscale* **2011**, *3*, 2054.

(10) Li, D.; Wang, C.; Strmcnik, D. S.; Tripkovic, D. V.; Sun, X.; Kang, Y.; Chi, M.; Snyder, J. D.; van der Vliet, D.; Tsai, Y.; Stamenkovic, V. R.; Sun, S.; Markovic, N. M. Functional Links between Pt Single Crystal Morphology and Nanoparticles with Different Size and Shape: The Oxygen Reduction Reaction Case. *Energy Environ. Sci.* **2014**, *7*, 4061−4069.

(11) Marković, N. M.; Adžić, R. R.; Cahan, B. D.; Yeager, E. B. Structural Effects in Electrocatalysis: Oxygen Reduction on Platinum Low Index Single-Crystal Surfaces in Perchloric Acid Solutions. *J. Electroanal. Chem.* **1994**, *377*, 249−259.

(12) Attard, G. A.; Brew, A.; Hunter, K.; Sharman, J.; Wright, E. Specific Adsorption of Perchlorate Anions on Pt{hkl} Single Crystal Electrodes. *Phys. Chem. Chem. Phys.* **2014**, *16*, 13689−13698.

(13) Furuya, N.; Shibata, M. Structural Changes at Various Pt Single Crystal Surfaces with Potential Cycles in Acidic and Alkaline Solutions. *J. Electroanal. Chem.* **1999**, *467*, 85−91.

(14) Herrero, E.; Buller, L. J.; Abruña, H. D. Underpotential Deposition at Single Crystal Surfaces of Au, Pt, Ag and Other Materials. *Chem. Rev.* **2001**, *101*, 1897−1930.

(15) Solla-Gullón, J.; Vidal-Iglesias, F. J.; López-Cudero, A.; Garnier, E.; Feliu, J. M.; Aldaz, A. Shape-Dependent Electrocatalysis: Methanol and Formic Acid Electrooxidation on Preferentially Oriented Pt Nanoparticles. *Phys. Chem. Chem. Phys.* **2008**, *10*, 3689.

(16) Cao, S.; Tao, F.; Tang, Y.; Li, Y.; Yu, J. Size- and Shape-Dependent Catalytic Performances of Oxidation and Reduction Reactions on Nanocatalysts. *Chem. Soc. Rev.* **2016**, *45*, 4747−4765.

(17) Bratlie, K. M.; Lee, H.; Komvopoulos, K.; Yang, P.; Somorjai, G. A. Platinum Nanoparticle Shape Effects on Benzene Hydrogenation Selectivity. *Nano Lett.* **2007**, *7*, 3097−3101.

(18) Kang, Y.; Li, M.; Cai, Y.; Cargnello, M.; Diaz, R. E.; Gordon, T. R.; Wieder, N. L.; Adzic, R. R.; Gorte, R. J.; Stach, E. A.; Murray, C. B. Heterogeneous Catalysts Need Not Be so "Heterogeneous": Monodisperse Pt Nanocrystals by Combining Shape-Controlled Synthesis and Purification by Colloidal Recrystallization. *J. Am. Chem. Soc.* **2013**, *135*, 2741−2747.

(19) Tian, N.; Zhou, Z.-Y.; Sun, S.-G.; Ding, Y.; Wang, Z. L. Synthesis of Tetrahexahedral Platinum Nanocrystals with High-Index Facets and High Electro-Oxidation Activity. *Science (Washington, DC, U. S.)* **2007**, *316*, 732−735.

(20) Xia, Y.; Xiong, Y.; Lim, B.; Skrabalak, S. E. Shape-Controlled Synthesis of Metal Nanocrystals: Simple Chemistry Meets Complex Physics? *Angew. Chem., Int. Ed.* **2009**, *48*, 60−103.

(21) Henzie, J.; Grünwald, M.; Widmer-Cooper, A.; Geissler, P. L.; Yang, P. Self-Assembly of Uniform Polyhedral Silver Nanocrystals into Densest Packings and Exotic Superlattices. *Nat. Mater.* **2012**, *11*, 131−137.

(22) Anderson, R. M.; Yancey, D. F.; Loussaert, J. A.; Crooks, R. M. Multistep Galvanic Exchange Synthesis Yielding Fully Reduced Pt Dendrimer-Encapsulated Nanoparticles. *Langmuir* **2014**, *30*, 15009−15015.

(23) Luo, L.; Zhang, L.; Duan, Z.; Lapp, A. S.; Henkelman, G.; Crooks, R. M. Efficient CO Oxidation Using Dendrimer-Encapsulated Pt Nanoparticles Activated with <2% Cu Surface Atoms. *ACS Nano* **2016**, *10*, 8760−8769.

(24) Lai, S. C. S.; Dudin, P. V.; MacPherson, J. V.; Unwin, P. R. Visualizing Zeptomole (Electro)Catalysis at Single Nanoparticles within an Ensemble. *J. Am. Chem. Soc.* **2011**, *133*, 10744−10747.

(25) Xiao, X.; Bard, A. J. Observing Single Nanoparticle Collisions at an Ultramicroelectrode by Electrocatalytic Amplification. *J. Am. Chem. Soc.* **2007**, *129*, 9610−9612.

(26) Xiao, X.; Fan, F.-R. F.; Zhou, J.; Bard, A. J. Current Transient in Single Nanoparticle Collision Events. *J. Am. Chem. Soc.* **2008**, *130*, 16669−16677.

(27) Li, Y.; Cox, J. T.; Zhang, B. Electrochemical Responses and Electrocatalysis at Single Au Nanoparticles. *J. Am. Chem. Soc.* **2010**, *132*, 3047−3054.

(28) Yu, Y.; Gao, Y.; Hu, K.; Blanchard, P. Y.; Noël, J. M.; Nareshkumar, T.; Phani, K. L.; Friedman, G.; Gogotsi, Y.; Mirkin, M. V. Electrochemistry and Electrocatalysis at Single Gold Nanoparticles Attached to Carbon Nanoelectrodes. *ChemElectroChem* **2015**, *2*, 58−63.

(29) Choi, M.; Siepser, N. P.; Jeong, S.; Wang, Y.; Jagdale, G.; Ye, X.; Baker, L. A. Probing Single-Particle Electrocatalytic Activity at Facet-Controlled Gold Nanocrystals. *Nano Lett.* **2020**, *20*, 1233−1239.

(30) Quast, T.; Varhade, S.; Saddeler, S.; Chen, Y.; Andronescu, C.; Schulz, S.; Schuhmann, W. Single Particle Nanoelectrochemistry Reveals the Catalytic Oxygen Evolution Reaction Activity of Co₃O₄ Nanocubes. *Angew. Chem., Int. Ed.* **2021**, *60*, 23444−23450.

(31) Shan, X.; Díez-Pérez, I.; Wang, L.; Wiktor, P.; Gu, Y.; Zhang, L.; Wang, W.; Lu, J.; Wang, S.; Gong, Q.; Li, J.; Tao, N. Imaging the Electrocatalytic Activity of Single Nanoparticles. *Nat. Nanotechnol.* **2012**, *7*, 668−672.

(32) Zhou, X.; Andoy, N. M.; Liu, G.; Choudhary, E.; Han, K.-S.; Shen, H.; Chen, P. Quantitative Super-Resolution Imaging Uncovers Reactivity Patterns on Single Nanocatalysts. *Nat. Nanotechnol.* **2012**, *7*, 237−241.

(33) Liu, P.; Qin, R.; Fu, G.; Zheng, N. Surface Coordination Chemistry of Metal Nanomaterials. *J. Am. Chem. Soc.* **2017**, *139*, 2122−2131.

(34) Zhao, S.; Jin, R.; Song, Y.; Zhang, H.; House, S. D.; Yang, J. C.; Jin, R. Atomically Precise Gold Nanoclusters Accelerate Hydrogen Evolution over MoS$_2$ Nanosheets: The Dual Interfacial Effect. *Small* **2017**, *13*, 1701519.

(35) Huang, K.; Clausmeyer, J.; Luo, L.; Jarvis, K.; Crooks, R. M. Shape-Controlled Electrodeposition of Single Pt Nanocrystals onto Carbon Nanoelectrodes. *Faraday Discuss.* **2018**, *210*, 267−280.

(36) Takahashi, Y.; Shevchuk, A. I.; Novak, P.; Zhang, Y.; Ebejer, N.; MacPherson, J. V.; Unwin, P. R.; Pollard, A. J.; Roy, D.; Clifford, C. A.; Shiku, H.; Matsue, T.; Klenerman, D.; Korchev, Y. E. Multifunctional Nanoprobes for Nanoscale Chemical Imaging and Localized Chemical Delivery at Surfaces and Interfaces. *Angew. Chem., Int. Ed.* **2011**, *50*, 9638−9642.

(37) Actis, P.; Tokar, S.; Clausmeyer, J.; Babakinejad, B.; Mikhaleva, S.; Cornut, R.; Takahashi, Y.; López Córdoba, A.; Novak, P.; Shevchuck, A. I.; Dougan, J. A.; Kazarian, S. G.; Gorelkin, P. V.; Erofeev, A. S.; Yaminsky, I. V.; Unwin, P. R.; Schuhmann, W.; Klenerman, D.; Rusakov, D. A.; Sviderskaya, E. V.; et al. Electrochemical Nanoprobes for Single-Cell Analysis. *ACS Nano* **2014**, *8*, 875−884.

(38) Zuo, J. M.; Gao, M.; Tao, J.; Li, B. Q.; Twesten, R.; Petrov, I. Coherent Nano-Area Electron Diffraction. *Microsc. Res. Tech.* **2004**, *64*, 347−355.

(39) Shah, A. B.; Sivapalan, S. T.; Devetter, B. M.; Yang, T. K.; Wen, J.; Bhargava, R.; Murphy, C. J.; Zuo, J. M. High-Index Facets in Gold Nanocrystals Elucidated by Coherent Electron Diffraction. *Nano Lett.* **2013**, *13*, 1840−1846.

(40) Clavilier, J.; Parsons, R.; Durand, R.; Lamy, C.; Leger, J. M. Formic Acid Oxidation on Single Crystal Platinum Electrodes. Comparison with Polycrystalline Platinum. *J. Electroanal. Chem. Interfacial Electrochem.* **1981**, *124*, 321−326.

(41) Ferre-Vilaplana, A.; Perales-Rondón, J. V.; Buso-Rogero, C.; Feliu, J. M.; Herrero, E. Formic Acid Oxidation on Platinum Electrodes: A Detailed Mechanism Supported by Experiments and Calculations on Well-Defined Surfaces. *J. Mater. Chem. A* **2017**, *5*, 21773−21784.

(42) Ye, J. Y.; Attard, G. A.; Brew, A.; Zhou, Z. Y.; Sun, S.-G.; Morgan, D. J.; Willock, D. J. Explicit Detection of the Mechanism of Platinum Nanoparticle Shape Control by Polyvinylpyrrolidone. *J. Phys. Chem. C* **2016**, *120*, 7532−7542.

(43) Gómez-Marín, A. M.; Feliu, J. M. Pt (111) Surface Disorder Kinetics in Perchloric Acid Solutions and the Influence of Specific Anion Adsorption. *Electrochim. Acta* **2012**, *82*, 558−569.

(44) Solla-Gullón, J.; Vidal-Iglesias, F. J.; Rodríguez, P.; Herrero, E.; Feliu, J. M.; Clavilier, J.; Aldaz, A. *In Situ* Surface Characterization of Preferentially Oriented Platinum Nanoparticles by Using Electrochemical Structure Sensitive Adsorption Reactions. *J. Phys. Chem. B* **2004**, *108*, 13573−13575.

(45) Wilde, P.; Quast, T.; Aiyappa, H. B.; Chen, Y.; Botz, A.; Tarnev, T.; Marquitan, M.; Feldhege, S.; Lindner, A.; Andronescu, C.; Schuhmann, W. Towards Reproducible Fabrication of Nanometre-Sized Carbon Electrodes: Optimisation of Automated Nanoelectrode Fabrication by Means of Transmission Electron Microscopy. *ChemElectroChem* **2018**, *5*, 3083−3088.

(46) Yu, Y.; Noël, J. M.; Mirkin, M. V.; Gao, Y.; Mashtalir, O.; Friedman, G.; Gogotsi, Y. Carbon Pipette-Based Electrochemical Nanosampler. *Anal. Chem.* **2014**, *86*, 3365−3372.

(47) Chen, S.; Kucernak, A. Electrodeposition of Platinum on Nanometer-Sized Carbon Electrodes. *J. Phys. Chem. B* **2003**, *107*, 8392−8402.

(48) Zhang, L.; Zhang, J.; Kuang, Q.; Xie, S.; Jiang, Z.; Xie, Z.; Zheng, L. Cu^{2+}-Assisted Synthesis of Hexoctahedral Au−Pd Alloy Nanocrystals with High-Index Facets. *J. Am. Chem. Soc.* **2011**, *133*, 17114−17117.

(49) Xiao, J.; Liu, S.; Tian, N.; Zhou, Z.-Y.; Liu, H.-X.; Xu, B.-B.; Sun, S.-G. Synthesis of Convex Hexoctahedral Pt Micro/Nanocrystals

with High-Index Facets and Electrochemistry-Mediated Shape Evolution. *J. Am. Chem. Soc.* **2013**, *135*, 18754−18757.

(50) Quan, Z.; Wang, Y.; Fang, J. High-Index Faceted Noble Metal Nanocrystals. *Acc. Chem. Res.* **2013**, *46*, 191−202.

(51) Huang, X.; Zhao, Z.; Fan, J.; Tan, Y.; Zheng, N. Amine-Assisted Synthesis of Concave Polyhedral Platinum Nanocrystals Having {411} High-Index Facets. *J. Am. Chem. Soc.* **2011**, *133*, 4718−4721.

(52) Santiago, U.; Velázquez-Salazar, J. J.; Sanchez, J. E.; Ruiz-Zepeda, F.; Ortega, J. E.; Reyes-Gasga, J.; Bazán-Díaz, L.; Betancourt, I.; Rauch, E. F.; Veron, M.; Ponce, A.; José-Yacamán, M. A Stable Multiply Twinned Decahedral Gold Nanoparticle with a Barrel-Like Shape. *Surf. Sci.* **2016**, *644*, 80−85.

(53) Mendoza-Cruz, R.; Romeu, D.; Bazán-Díaz, L.; Samaniego, J. E.; Santiago, U.; Ponce, A.; José-Yacamán, M. Evaporation of Gold on NaCl Surfaces as a Way to Control Spatial Distribution of Nanoparticles: Insights on the Shape and Crystallographic Orientation. *Cryst. Growth Des.* **2017**, *17*, 6062−6070.

(54) Grozovski, V.; Solla-Gullón, J.; Climent, V.; Herrero, E.; Feliu, J. M. Formic Acid Oxidation on Shape-Controlled Pt Nanoparticles Studied by Pulsed Voltammetry. *J. Phys. Chem. C* **2010**, *114*, 13802−13812.

(55) Chen, Q. S.; Zhou, Z. Y.; Vidal-Iglesias, F. J.; Solla-Gullón, J.; Feliu, J. M.; Sun, S.-G. Significantly Enhancing Catalytic Activity of Tetrahexahedral Pt Nanocrystals by Bi Adatom Decoration. *J. Am. Chem. Soc.* **2011**, *133*, 12930−12933.

(56) Clavilier, J.; Armand, D.; Sun, S. G.; Petit, M. Electrochemical Adsorption Behaviour of Platinum Stepped Surfaces in Sulphuric Acid Solutions. *J. Electroanal. Chem. Interfacial Electrochem.* **1986**, *205*, 267−277.

(57) Zhang, L.; Chen, D.; Jiang, Z.; Zhang, J.; Xie, S.; Kuang, Q.; Xie, Z.; Zheng, L. Facile Syntheses and Enhanced Electrocatalytic Activities of Pt Nanocrystals with {hkk} High-Index Surfaces. *Nano Res.* **2012**, *5*, 181−189.

(58) Grozovski, V.; Climent, V.; Herrero, E.; Feliu, J. M. Intrinsic Activity and Poisoning Rate for HCOOH Oxidation at Pt(100) and Vicinal Surfaces Containing Monoatomic (111) Steps. *ChemPhysChem* **2009**, *10*, 1922−1926.

(59) Sun, S.-G.; Yang, Y. Y. Studies of Kinetics of HCOOH Oxidation on Pt(100), Pt(110), Pt(111), Pt(510) and Pt(911) Single Crystal Electrodes. *J. Electroanal. Chem.* **1999**, *467*, 121−131.

(60) Briega-Martos, V.; Solla-Gullón, J.; Koper, M. T. M.; Herrero, E.; Feliu, J. M. Electrocatalytic Enhancement of Formic Acid Oxidation Reaction by Acetonitrile on Well-Defined Platinum Surfaces. *Electrochim. Acta* **2019**, *295*, 835−845.

(61) Li, Y.; Jiang, Y.; Chen, M.; Liao, H.; Huang, R.; Zhou, Z.; Tian, N.; Chen, S.; Sun, S.-G. Electrochemically Shape-Controlled Synthesis of Trapezohedral Platinum Nanocrystals with High Electrocatalytic Activity. *Chem. Commun.* **2012**, *48*, 9531.

(62) Lu, B.-A.; Du, J.-H.; Sheng, T.; Tian, N.; Xiao, J.; Liu, L.; Xu, B.-B.; Zhou, Z.-Y.; Sun, S.-G. Hydrogen Adsorption-Mediated Synthesis of Concave Pt Nanocubes and Their Enhanced Electrocatalytic Activity. *Nanoscale* **2016**, *8*, 11559−11564.

(63) Schwarz, K. A.; Sundararaman, R.; Moffat, T. P.; Allison, T. C. Formic Acid Oxidation on Platinum: A Simple Mechanistic Study. *Phys. Chem. Chem. Phys.* **2015**, *17*, 20805−20813.

(64) Chen, Q. S.; Berna, A.; Climent, V.; Sun, S.-G.; Feliu, J. M. Specific Reactivity of Step Sites towards CO Adsorption and Oxidation on Platinum Single Crystals Vicinal to Pt(111). *Phys. Chem. Chem. Phys.* **2010**, *12*, 11407−11416.

(65) Chang, S. C.; Leung, L. W. H.; Weaver, M. J. Metal Crystallinity Effects in Electrocatalysis as Probed by Real-Time FTIR Spectroscopy: Electrooxidation of Formic Acid, Methanol, and Ethanol on Ordered Low-Index Platinum Surfaces. *J. Phys. Chem.* **1990**, *94*, 6013−6021.

(66) Ostojic, N.; Duan, Z.; Galyamova, A.; Henkelman, G.; Crooks, R. M. Electrocatalytic Study of the Oxygen Reduction Reaction at Gold Nanoparticles in the Absence and Presence of Interactions with SnO$_x$ Supports. *J. Am. Chem. Soc.* **2018**, *140*, 13775−13785.

(67) Ferrin, P.; Nilekar, A. U.; Greeley, J.; Mavrikakis, M.; Rossmeisl, J. Reactivity Descriptors for Direct Methanol Fuel Cell Anode Catalysts. *Surf. Sci.* **2008**, *602*, 3424−3431.

(68) Jung, I.; Shin, K.; Kim, N. R.; Lee, H. M. Synthesis of Low-Temperature-Processable and Highly Conductive Ag Ink by a Simple Ligand Modification: The Role of Adsorption Energy. *J. Mater. Chem. C* **2013**, *1*, 1855−1862.